CCS Chemistry

IMMEDIATE ONLINE ACCEPTED (IOA) ARTICLE

IOA Posting Date: August 07, 2023

TITLE: Achieving High CO_2 Photoreduction Activity by Conductive Crosslinks of Metal-Organic framework

AUTHORS: Ning Li, Gui-Qi Lai, Lai-Hon Chung, Fei Yu, Jun He and Ya-Qian Lan

DOI: 10.31635/ccschem.023.202303055

CITE THIS: *CCS Chem.* **2023**, Just Accepted. DOI: 10.31635/ccschem.023.202303055

Achieving High CO_2 Photoreduction Activity by Conductive Crosslinks of Metal-Organic framework

Ning Li[1], Gui-Qi Lai[1], Lai-Hon Chung[1], Fei Yu[3], Jun He[1]* and Ya-Qian Lan[2]*

[1]Department School of Chemical Engineering and Light Industry, Guangdong University of Technology, Guangzhou, Guangdong 510006

[2]School of Chemistry, South China Normal University, Guangzhou 510006

[3]School of Chemistry and Materials Science, Nanjing Normal University, Nanjing 210023

*Corresponding Authors: He Jun: junhe@gdut.edu.cn; Lan Ya-Qian: yqlan@m.scnu.edu.cn

Abstract

Fast photogenerated charge migration is crucial for the improvement of photocatalytic performance but is difficult to be deliberately modulated. This work presents two Zr-based metal-organic framework catalysts, **GDUT-8** and **GDUT-8-Ox**, for photocatalytic CO_2 reduction reaction. Specifically, thiophene pendants in **GDUT-8** were coupled covalently *via* Scholl reaction to give **GDUT-8-Ox** along with conductivity enhanced by at least two orders of magnitude (up to 6.1×10^{-3} S cm^{-1}) and hence faster transport of photogenerated carriers during photocatalysis. Furthermore, from **GDUT-8** to **GDUT-8-Ox**, stronger ligand-to-cluster charge transfer with pronounced light absorption extension was observed. As a result, **GDUT-8-Ox** exhibited the highest photocatalytic CO_2-to-$HCOO^-$ conversion rate (1725 μmol g^{-1} h^{-1}) to date, in the absence of photosensitizer, as well as TON, TOF and quantum efficiency much higher than **GDUT-8**. This work presents an unprecedented strategy to accelerate the photogenerated carriers transport of photocatalysts.

Keywords

metal-organic framework, Scholl reaction, covalent crosslinks, high conductivity, CO_2 photoreduction, CO_2-to-$HCOO^-$ conversion

Introduction

Solar-driven photochemical reduction of CO_2 to usable chemicals is recognized as one of the most promising technologies for sustainable carbon recycling.[1-7] By the effort in decades, it was found that parameters governing photocatalytic performance should be considered for design of photocatalysts to achieve highly selective and effective CO_2 conversion.[8-10] Specifically, competent photocatalysts should possess the following features: (i) effective active site (for adsorption and activation of CO_2);[11-15] (ii) good light-harvesting capability (dictating solar energy utilization efficiency);[16,17] (iii) tunable functionalities (for modulation of band structure/highest occupied molecular orbital-lowest unoccupied molecular orbital, HOMO-LUMO, energy level distribution);[18-21] (iv) prompt transfer of photogenerated charges (attaining high catalytic rate by suppression of electron-hole, e^--h^+, pair recombination).[9, 15, 22] Out of various materials, metal-organic frameworks (MOFs) arise as ideal candidates for photocatalysis owing to their unambiguous structure, tailorable functionalities, *etc.* and have been proven to be outstanding in modulation of photocatalytic activity *via* rich structural regulation.[23-27]

Numerous studies on light-driven CO_2 reduction reaction (CO_2RR) by MOF catalysts reveal that right combination of metal nodes and functionalized linkers leads to framework with effective active sites and decent light-harvesting capability.[28, 29] Upon broad spectrum of irradiation, the MOF catalysts exhibit higher selectivity of CO_2RR to specific products (*e.g.*, CO, HCOOH). However, generally inherent poor electrical conductivity in MOF catalysts always results in slow transfer of photogenerated charge carriers and hence limited quantum efficiency as well as low CO_2RR rate.[30, 31] Unfortunately, there is still a lack of solutions to tackle this issue so far. Noteworthy, oxidative coupling of thiophene and its derivatives to polythiophenes represents one of the most commonly used strategies to generate materials with high electrical conductivity.[32-34] In this regard, constructing polythiophene within framework may turn to be a viable strategy to enhance the inherent electrical conductivity of MOF catalysts and hence the transport of photogenerated charge carriers for boosting CO_2 photoreduction.

As a proof-of-concept study, we designed and constructed a Zr-based MOF catalyst, **GDUT-8,** assembled from $[Zr_6O_8]$ nodes and H_2**BPD-4F4TS** linkers (2,2',5,5'-tetrafluoro-3,3',6,6'-tetrakis(2-thiophenethio)-4,4'-biphenyl dicarboxylic acid), for light-driven CO_2 reduction. **GDUT-8** shows high structural stability, and the large ionic radius and high coordination number of Zr^{4+} center in Zr–O cluster can create ample space and catalytic site for the adsorption and subsequent photo-activation of CO_2 molecules. Notably, near-neighbouring thiophenes pendants in **GDUT-8** can be bonded through Scholl reaction to give crystalline framework bearing coupled thiophene linkers, **GDUT-8-Ox**. Importantly, **GDUT-8-Ox** exhibits electrical conductivity of 6.1×10^{-3} S cm^{-1}, better than **GDUT-8** (2.3×10^{-5} S cm^{-1}) by at least two orders of magnitude. Furthermore, **GDUT-8-Ox** showed more pronounced ligand-to-cluster charge transfer (LCCT) with extension of absorption profile from ending at 400 nm (UV region) to ending at 800 nm (covering the whole visible spectral region) when compared with **GDUT-8**. Based on the above betterment by thiophene coupling, **GDUT-8-Ox** achieved highly selective CO_2-to-$HCOO^-$ conversion (*i.e.*, selectivity to $HCOO^-$ of 100%) together with improved catalytic activity than primitive **GDUT-8** as reflected by higher conversion rate of HCOOH (from 553 μmol g^{-1} h^{-1} to 1078 μmol g^{-1} h^{-1}), turnover numbers (TON, from 21.88 to 50.93), turnover frequencies (TOF, from 10.94 h^{-1} to 25.47 h^{-1}) and quantum efficiency (from 0.009% to 0.018%) under visible light irradiation. Theoretical calculation reveals that lower kinetic barrier for rate-determining *COOH intermediate formation is observed in **GDUT-8-Ox** than **GDUT-8** and therefore contributes to faster catalysis along with prompt HCOOH production. The better photocatalytic performance by **GDUT-8-Ox** probably originates from the elevated mobility of photogenerated charge carriers. More importantly, this work represents the first example of boosting photocatalytic CO_2RR by improving the transport rate of photogenerated charge carriers/suppressing electron-hole (e^--h^+) pair recombination of MOFs *via* electrical conductivity enhancement.

Experimental Methods

Materials

All starting materials, reagents and solvents used in experiments were commercially available, high-grade purity materials and used without further purification. 2-Thiophene thiol and Nitromethane were purchased from Aladdin, $ZrCl_4$ was purchased from Acros, Trifluoroacetic acid, I_2, K_2CO_3, NaOH, Ethanol (EtOH), N,N-Dimethylformamide (DMF) were purchased from Admas, Toluene, Acetone were purchased from Guangzhou Chemical reagents.

Synthesis Method of GDUT-8

H_2BPD-4F4TS (540 mg, 0.71 mmol), $ZrCl_4$ (400 mg, 1.72 mmol), trifluoroacetic acid (245.6 mg, 2.15 mmol) and dry DMF (4 mL) were added to a glass vial (10 ml) with the aluminum cap. After sonication for 5 min to form a light-yellow solution, the reaction was carried out at 120 °C for 4 days. After cooling to room temperature, the solution was washed with DMF and acetone and filtered to obtain colorless polyhedral crystals. Elemental analysis found [C (36.85%), H (1.86%), S (23.05%), N (0.82%)], a fitting formula can be determined to be $Zr_6O_4(OH)_4(C_{30}H_{12}F_4O_4S_8)_{2.9}(HCOO)_{6.2}(H_2O)_8(DMF)_2$ (mw. 3230)

Synthesis Method of GDUT-8-Ox

GDUT-8 crystals (10 mg), I_2 (31 mg, 0.12 mmol) and n-hexane (5 mL) were added to a 50 mL Schlenk tube. After sonication and dispersion, the reaction solution is heated through an oil bath (90°C) for 12 hours. After the reaction, the crystals were filtered and washed several times with hexane and acetone until the solution became colourless. The oxidized crystals were then further subjected to acetone soxhlet extraction for 1 day and dried to give brown crystals of the as-made **GDUT-8-Ox**.

Photocatalytic CO_2 reduction test

Photocatalytic reduction of CO_2 was performed in a 50 mL Schlenk tube with as-prepared crystal. Photocatalyst (5mg) was added into the mixed solution which contained H_2O (28 mL) and trietanolamina (TEOA, 2mL) as an electron donor. After degassing with high-purity CO_2 to remove dissolved O_2 for 30 min, the reaction was performed under the irradiation of a 300 W Xe lamp with UV and IR-cut to keep the wavelengths in the range from 420 to 800 nm. The reaction temperature was controlled at 303 K by using the cooling water circulation. The photocatalytic gas-phase products (CO, CH_4, H_2, O_2) were analyzed by Agilent

Gas Chromatography equipped a flame ionization detector (FID) with methanizer and a thermal conductivity detector (TCD). 500 μL of gas-product was extracted from the reactor with a syringe and injected into the gas chromatograph with a flame ionization detector (FID), using nitrogen as the carrier gas and reference gas. The liquid products ($HCOO^-$) in the liquid phase of the reactor were measured using ion chromatography (IC). The flow velocity of the IC mobile phase was 1 mL/min, and the sampling volume of the automatic injection syringe was 25 μL (the injection needle needs to be washed three times with deionized water between different standards, and the needle is rinsed in water before it withdraws samples). The solution obtained after photocatalysis was filtered with a filter head (0.22 μm) and a syringe was used to obtain a clear solution of the filtrate. 1 ml of the filtrate is collected and diluted 100 times with a 100 ml volumetric flask. By comparing the peak area of the liquid-phase product with the standard curve, the volume of the liquid-phase product $HCOO^-$ can be calculated.

Electrochemistry measurements

All electrochemical measurements (photocurrent and EIS) were carried out with a CHI 660E electrochemical workstation via a conventional three-electrode system in a 0.5 M Na_2SO_4 aqueous solution. The working electrode was ITO glass plates coated with a catalyst-slurry, the counter electrode was a platinum foil, and the reference electrode was a saturated Ag/AgCl electrode. Electrochemical impedance spectra (EIS) measurements were recorded over a frequency range of 100 kHz–0.1 Hz, and 0.5 M Na_2SO_4 aqueous solution was used as the supporting electrolyte. Preparation of the working electrode: 2 mg photocatalysts were dispersed in a mixed solution of 990 μL ethanol and 10 μL Nafion D-520 dispersion solutions to generate a homogeneous slurry. Subsequently, 100 μL of slurry was transferred and coated on ITO glass plates (1 cm × 1 cm) then dried at room temperature. The Ag/AgCl electrode was employed as the reference electrode, and platinum plate was used as the counter electrode, respectively.

Results and Discussion

Structures and Characterizations of GDUT-8 and GDUT-8-Ox

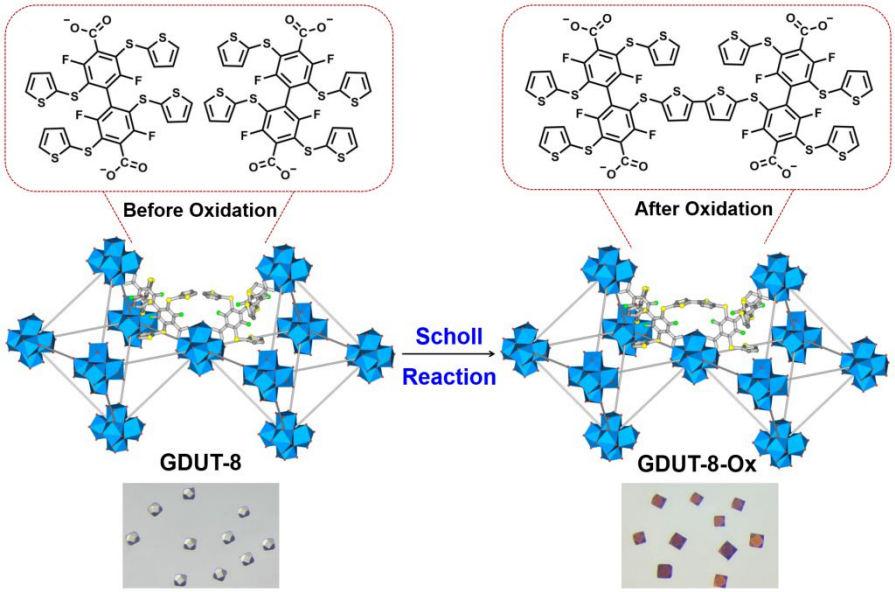

Scheme 1. View of the preparation of **GDUT-8** and its conversion into **GDUT-8-Ox** through the couplings among near-neighbouring thiophenes.

Solvothermal reaction between $ZrCl_4$ and H_2**BPD-4F4TS** (Fig. S1-S7) in sealed glass bottle at 120 °C for 72 h gave **GDUT-8** as colourless octahedral crystals (Fig. S8). The single crystal obtained has a UiO-67 type network structure (Fig. S9-S12, Table S1-S3). With optimized self-assembly conditions, **GDUT-8** crystals of good quality were isolated and taken for single-crystal X-ray diffraction (SCXRD) data collection. SCXRD analysis shows that **GDUT-8** adopts the cubic space group $Pm\bar{3}m$ (No. 221), consisting of a face-centred-cubic array of $[Zr_6O_4(OH)_4]$ clusters connected to carboxylate units of the **BPD-4F4TS**$^{2-}$ linker to yield the **fcu** topology of the prototype UiO-67 framework.[35] It is noteworthy that the thiophene groups on the linkers within the Zr_6 cluster-based octahedral cage in **GDUT-8** are difficult to be coupled due to long distance and inappropriate spatial arrangement. By contrast, the close proximity between thiophene groups on adjacent linkers from two neighbouring octahedral cages highlights the possibility of oxidative thiophene coupling to give conjugated crosslinks (Fig. 1a-f). The free solvent was excluded and the porosity of **GDUT-8** was obtained by PLATON calculations to be about 48.4%. Upon oxidation treatment, colourless **GDUT-8** darkened (**Scheme 1**

and Fig. S8) and the resultant black solids were denoted as **GDUT-8-Ox**. As expected, **GDUT-8-Ox** crystallizes in the same cubic space group $Pm\bar{3}m$, and keeps the pristine **GDUT-8** framework but with oxidative coupling between thiophene moieties on adjacent linkers from two neighbouring octahedral cages.

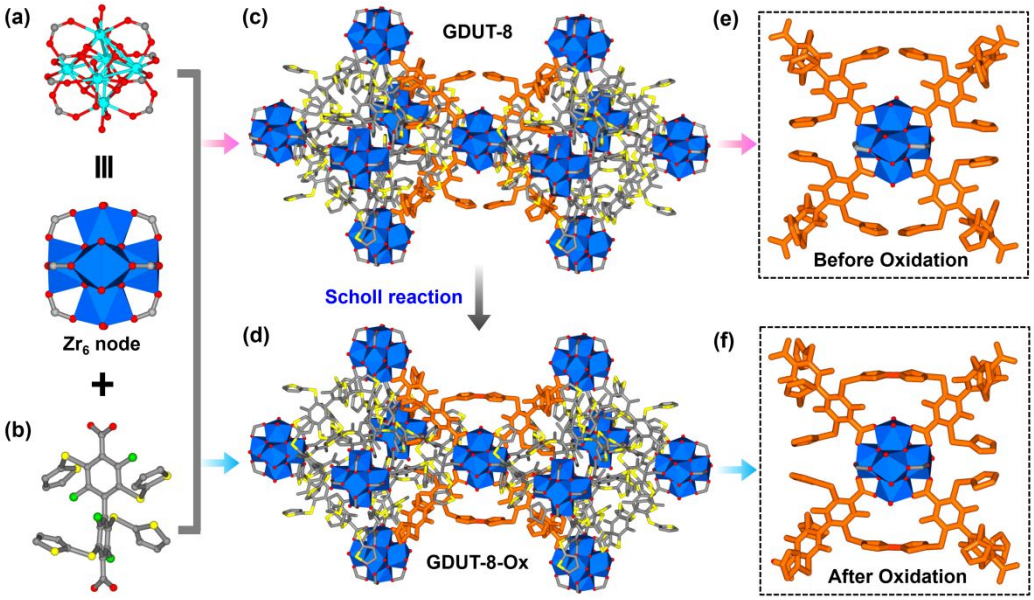

Fig.1. Construction of (c) **GDUT-8** from (a) $[Zr_6O_4(OH)_4]$ clusters linked by (b) organic linker H_2**BPD-4F4TS**; (d) Structure view of **GDUT-8-Ox** converted from **GDUT-8;** (e, f) Enlarged view of the organic linkers in **GDUT-8** and **GDUT-8-Ox.**

Crystal morphology of these two MOFs can be observed from scanning electron microscopy (SEM) characterization (Fig. S13-S15). Consistent powder X-ray diffraction (PXRD) patterns of **GDUT-8-Ox** and **GDUT-8** also suggest that the parent metal-organic framework keeps intact throughout oxidation (Fig. S16). The N_2 sorption isotherm of **GDUT-8** at 77 K features a type II isotherm accompanied by a hysteresis loop (Fig. S17-S20). The Brunauer-Emmett-Teller (BET) surface area of **GDUT-8** calculated from the sorption isotherms is 531.60 $m^2 g^{-1}$. On the other hand, the N_2 sorption isotherm of **GDUT-8-Ox** at 77 K is characteristic of a type III isotherm and shows a hysteresis loop (Fig. S21-S24). The hysteresis loops may stem from the blockage of N_2 by the thiophene ring in the pore channel during N_2 desorption. Enhanced thermal stability of **GDUT-8-Ox**

over **GDUT-8** as reflected by their thermogravimetric analysis (TGA) profiles (*i.e.*, steep weight loss in **GDUT-8** at ~300 °C *vs.* weight loss in **GDUT-8-Ox** starting at > 350 °C, Fig. S25 and S26). We have also further verified the solubility decrease of linker from **GDUT-8** to **GDUT-8-Ox.** The activated crystals of **GDUT-8** digested in DCl/NaF/DMSO-d_6 for ^{1}H and ^{19}F nuclear magnetic resonance, NMR, spectroscopy and indicated the presence of H_2**BPD-4F4TS**, (Fig. S27 and S28), while **GDUT-8-Ox** failed to digest in the same concentration of DCl/NaF/DMSO-d_6 unless the concentration of HF is increased and stirred at 85°C for 4h. Comparison between the ^{1}H NMR spectra of digested **GDUT-8** and **GDUT-8-Ox** (Fig. S29- S31) shows that the characteristic peaks of **GDUT-8-Ox** are broader and the H-atom ratio is not consistent with that of the ligand compared to the almost indistinguishable sharp peaks of **GDUT-8**, consolidating reduced solubility of the linkers in **GDUT-8-Ox**. Also, the broadening of the shoulder peak of the C atom from the coupling site in the solid ^{13}C NMR spectrum of the oxidized **GDUT-8-Ox** reveals that some C–H bonds joined to give C–C bonds through oxidative coupling (Fig. S32). All the above results suggest that structural robustness of linkers in **GDUT-8** improve after oxidation. More importantly, the enhancement of electrical conductivity by two orders of magnitude from **GDUT-8** (2.3×10^{-5} S cm^{-1}) to **GDUT-8-Ox** (6.1×10^{-3} S cm^{-1}) also supports that coupling of adjacent thiophenes to give electronically more conjugated moieties (Fig. S33, Table S4).

GDUT-8-Ox with darkened appearance (Fig. S8) have red-shift in absorption. As shown in Fig. 2a, **GDUT-8** absorbs strongly in ultraviolet (UV) region, 200–400 nm, with negligible absorption in visible spectral region while **GDUT-8-Ox** exhibits absorption almost covering the whole UV-vis spectral region (tailing until 800 nm). The optical absorption of **GDUT-8** and **GDUT-8-Ox** mainly from the electron transition, which from the thiophene chromophore to the Zr–O clusters, *i.e.,* LCCT.[36-38] Sensibly, the enhanced electronic conjugation after thiophene coupling narrows the $\pi \rightarrow \pi^*$ gap and accelerates the rate of electron transfer during LCCT, which results in the red-shift of the **GDUT-8-Ox** absorption spectrum after thiophene coupling and improves its light absorption in the visible region.[13] The optical band gaps of **GDUT-8** and **GDUT-8-Ox** were calculated to be 2.98 and 1.93 eV respectively, from the Tauc plot using the Kubelka-Munk function (Fig. 2b). We

performed ultraviolet photoelectron spectroscopy (UPS) to determine the highest occupied molecular orbital (HOMO) energy levels of the MOFs (Fig. 2c and 2d). The HOMO energy levels of **GDUT-8** and **GDUT-8-Ox** are 6.24 (1.39 V *vs.* NHE) and 5.74 eV (0.89 V *vs.* NHE), respectively. On this basis, the corresponding lowest unoccupied molecular orbital (LUMO) energy levels of **GDUT-8** and **GDUT-8-Ox** can be obtained by E_v-E_g calculation as 3.26 (–1.59 V *vs.* NHE) and 3.81 eV (–1.04 V *vs.* NHE), respectively. Higher lying LUMOs than the reduction potential required for reduction of CO_2 to various products ($HCOO^-$, –0.61 V; CO, –0.51 V; CH_4, –0.24 V *vs.* NHE at pH = 7, [39] Fig. 2e) features both **GDUT-8** and **GDUT-8-Ox** as promising candidates in CO_2 reduction. As shown in the Nyquist plots of electrochemical impedance spectroscopy (EIS), smaller arc radius of **GDUT-8-Ox** than **GDUT-8** (Fig. 2f) indicates lower charge transfer resistance in **GDUT-8-Ox** than **GDUT-8**, *i.e.*, more efficient charge flow. The smaller charge transfer resistance of **GDUT-8-Ox** comes from the stronger electronic conjugation given by coupled thiophene moieties. This is one of the reasons why **GDUT-8-Ox** has a less negative LUMO energy level.

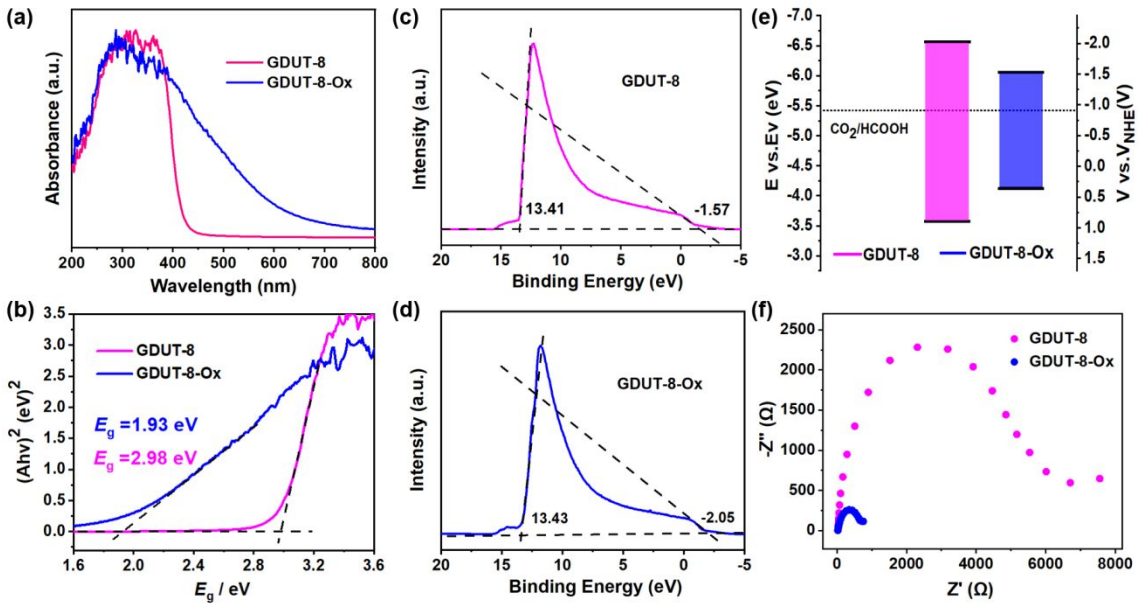

Fig.2. (a) Solid-state UV–vis absorption spectra of **GDUT-8** and **GDUT-8-Ox**. (b) Tauc plots of **GDUT-8** and **GDUT-8-Ox**. UPS spectra of (c) **GDUT-8** and (d) **GDUT-8-Ox.** (e) Energy band structure diagram for **GDUT-8** and **GDUT-8-Ox**. (f) Electrochemical impedance spectra of **GDUT-8** and **GDUT-8-Ox.**

Photochemical CO2 Reduction Performance

After oxidative coupling of thiophene, significant absorption red shift and electrical conductivity improvement make **GDUT-8-Ox** an ideal candidate for verifying how elevated mobility of photogenerated charge carriers promotes photocatalytic CO_2RR. Therefore, **GDUT-8** and **GDUT-8-Ox** were used as catalysts for photocatalytic CO_2RR using H_2O as solvent, triethanolamine (TEOA) as sacrificial agent and a Xenon lamp as irradiation source without addition of external photosensitizers (Fig. S34). As shown in the Fig. 3a, the $HCOO^-$ yields of **GDUT-8** and **GDUT-8-Ox** can reach 858 and 1725 μmol g^{-1} h^{-1}, highlighting **GDUT-8-Ox** to be still more superior than **GDUT-8** in terms of photocatalytic power. Higher photocatalytic activity of **GDUT-8-Ox** here most likely results from stronger absorptivity in visible spectral region. To further demonstrate that the enhanced photocatalytic performance is related to increased mobility of photogenerated charge carriers, the photocatalytic performance of **GDUT-8** and **GDUT-8-Ox** were studied the same conditions only with UV-light replaced by visible light source, thus excluding the effect of stronger absorptivity of visible light on the performance. As can be seen from the Fig. 3b, the $HCOO^-$ yields of **GDUT-8** and **GDUT-8-Ox** can reach 549 and 1050 μmol g^{-1} h^{-1} after 2 h of reaction under visible light irradiation, respectively. It can be concluded that the improved photocatalytic performance of the MOF catalyst after oxidative coupling comes from increased mobility of photogenerated charge carriers and extended absorption covering the whole visible spectral region.

In this study, the yield of $HCOO^-$ was detected by ion chromatography (IC) (Fig. 3c) and the gas phase products were detected by gas chromatography (GC). No gas products detected from photocatalytic CO_2RR by **GDUT-8** and **GDUT-8-Ox** (Fig. S35 and S36) indicate that the CO_2RR proceeds through CO_2-to-$HCOO^-$ conversion with absolute selectivity. In addition, to investigate the catalytic performance with respect to active centres in **GDUT-8** and **GDUT-8-Ox**, the corresponding TON and TOF were calculated (Table S5). The catalytic site activity, TON_{Zr}, was found to be 21.88 for **GDUT-8** and 50.93 for **GDUT-8-Ox** signifying **GDUT-8-Ox** as a better photocatalyst than **GDUT-8**. During the photocatalytic reaction, the photogenerated

e^- flow to the Zr–O cluster *via* LCCT, and the TON_{Zr} and TOF results further illustrate that **GDUT-8-Ox** has more efficient transport of photogenerated charge carriers, which is thus manifested as increased activity of the catalytic site.

Moreover, no $HCOO^-$ was detected when the photocatalytic CO_2RR were carried out under one of the following conditions (Table S6): (1) no photocatalyst added; (2) no irradiation; (3) linkers replacing MOFs as catalysts; (4) Ar in place of CO_2. These results signify that all these conditions are compulsory for CO_2RR to proceed. Also, experiments using $^{13}CO_2$ as reactant gas were conducted to verify the source of carbon in $HCOO^-$. ^{13}C NMR spectra of the filtrate collected from CO_2RR photocatalyzed by both **GDUT-8** and **GDUT-8-Ox** show peaks of $HCOO^-$ at 165 ppm in DMSO-d_6 (Fig. S37 and S38) which are negligible in the results using $^{12}CO_2$ as reaction atmosphere (Fig. S39 and S40).[40, 41] These results tell that detected $HCOO^-$ indeed comes from CO_2. Besides, the UV-vis absorption profiles of the filtrate after photocatalytic CO_2RR by **GDUT-8** and **GDUT-8-Ox** do not show signals corresponding to detached linkers (Fig. S41 and S42), meaning that both **GDUT-8** and **GDUT-8-Ox** keep intact throughout the catalytic reaction echoing their unchanged PXRD patterns collected before and after catalysis (Fig. S43). The results showed that the FTIR spectra of **GDUT-8** and **GDUT-8-Ox** are basically the same as those before the reaction which eliminates the possibility of decomposition of the catalyst during the reaction (Fig. S44 and S45). Noteworthy, no significant change in $HCOO^-$ yield of CO_2RR for three cycles using both **GDUT-8** and **GDUT-8-Ox** highlights the robust catalytic activity and recyclability of these MOFs (Fig. 3d).

To further compare and rationalize the difference in photocatalytic activity between **GDUT-8** and **GDUT-8**, various characterization techniques were employed. The results of the transient photocurrent response measurement show that (Fig. 3e) greater photocurrent response in **GDUT-8-Ox** than **GDUT-8** confirms larger amount of charge carrier and more efficient separation of photogenerated e^--h^+ pair in **GDUT-8-Ox** than **GDUT-8**. EIS characterization finding echoes the results of transient photocurrent response measurement and again validates enhanced charge flow efficiency as the contributor for higher photocatalytic activity. In

addition, photoluminescence (PL) measurement was also used to study the separation of the photogenerated e^--h^+ pair. Under 350 nm photoexcitation, **GDUT-8** emits at λ_{em} = 540 nm, while **GDUT-8-Ox** shows a much weaker photoluminescence peak at λ_{em} = 540 nm (Fig. S46) suggesting more facile drainage of photogenerated e^- in **GDUT-8-Ox** than **GDUT-8-Ox**. Longer excited-state lifetime (λ_{em} = 540 nm) of **GDUT-8-Ox** (7.33 ns) than **GDUT-8** (5.25 ns) (Fig. S47) means more persistent excited state (e^--h^+ separation state) in **GDUT-8-Ox** than **GDUT-8**. The separation of photogenerated e^--h^+ is therefore more complete for **GDUT-8-Ox**, in accordance with the results of the PL measurement.

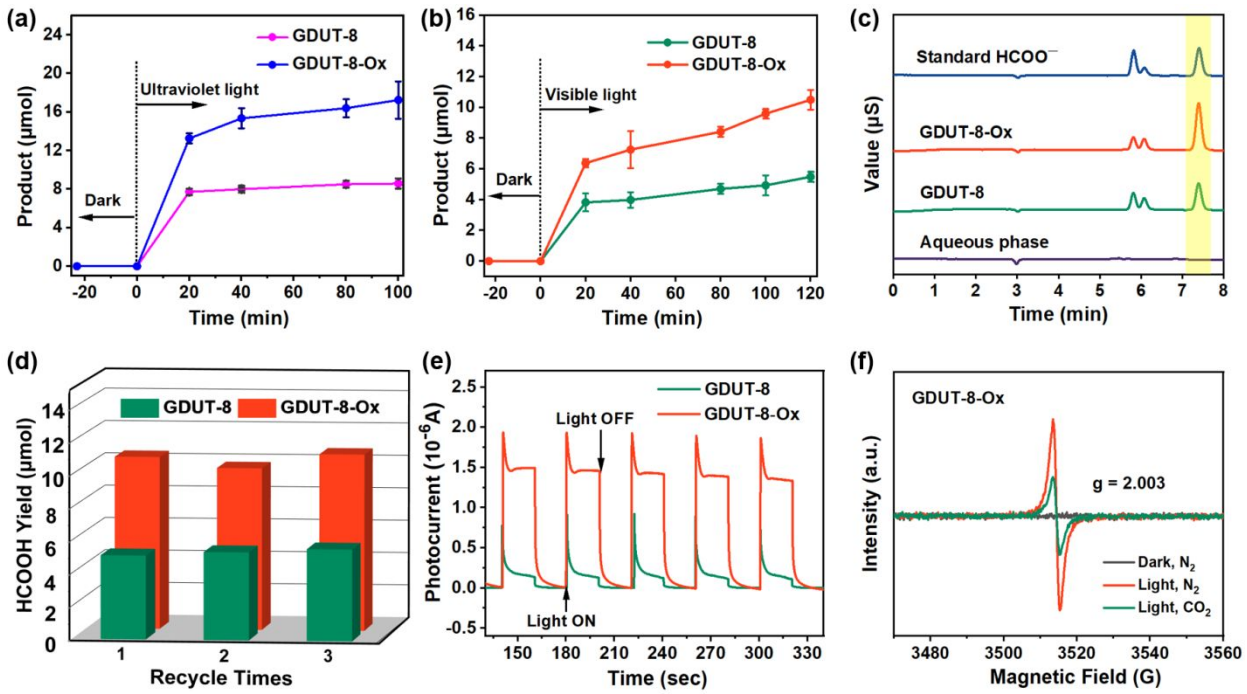

Fig.3. Amount of $HCOO^-$ produced by **GDUT-8** and **GDUT-8-Ox** under (a) ultraviolet light and (b) visible light over time. (c) Analysis of the liquid reaction products generated in photocatalytic system by ion chromatography. (d) The recycling of **GDUT-8** and **GDUT-8-Ox** for CO_2 photoreduction. (e) Transient photocurrent responses of **GDUT-8** and **GDUT-8-Ox** under visible light irradiation. (f) EPR spectra of **GDUT-8-Ox.**

Noteworthy is that the apparent quantum efficiency (AQE) of **GDUT-8-Ox** (0.018%–0.02%) regardless of the irradiation wavelengths (380, 420 or 520 nm) (Table S7 and S8) were higher than the AQE of **GDUT-8**

(0.009%–0.017%). The AQE of **GDUT-8-Ox** (0.020% or 0.021%) is about 1.2 times higher than that of **GDUT-8** (0.017%) when irradiated at 380 or 420 nm. Better light utilization again demonstrates the increased photogenerated charge flow rate of **GDUT-8-Ox** after oxidation. At irradiation of 520 nm, the AQE of **GDUT-8-Ox** (0.018%) is twice as high as that of **GDUT-8** (0.009%). Such an enhancement of light utilization in **GDUT-8-Ox** is attributed to its stronger absorptivity in the visible spectral region.

Reaction Mechanism, DFT Calculations and In situ Characterization

Electron paramagnetic resonance (EPR) spectroscopy was employed to study the mechanism of photocatalyzed CO_2RR, with **GDUT-8-Ox** as representative sample. Without light irradiation under N_2 atmosphere, the photocatalyst did not show EPR signals (Fig. 3f). Upon light irradiation under N_2 atmosphere, sharp signals corresponding to Zr^{III} species in **GDUT-8-Ox** emerged.[11] After photoexcitation, Zr^{IV} in the Zr–O cluster accepts electrons from the linkers to form Zr^{III}, generating the EPR signal. This verifies the flow of e^- from the linkers to the Zr–O cluster through LCCT upon light irradiation.[38] On the other hand, the EPR signal of photocatalyst weakened under continuous light irradiation (1 h) under CO_2 atmosphere, suggesting the involvement of Zr^{III} species in the photo-driven CO_2RR. The photoexcitation can be rationalized as follows: upon light irradiation, e^- migrate from the photoexcited linker to the Zr–O cluster and reduce the Zr^{IV} species to the Zr^{III} species, while the TEOA acts as a h^+ scavenger. After the introduction of CO_2, e^- are transferred from the Zr^{III} species to CO_2, in parallel with the conversion of the Zr^{III} species to the Zr^{IV} species (manifested as a weakening of the EPR signal). Thus, photocatalytic cycle of CO_2-to-$HCOO^-$ conversion is achieved.

To gain more insight, the electron-hole Coulomb attraction energy (E_c) in the first excited state was calculated to probe the charge separation efficiency of **GDUT-8** and **GDUT-8-Ox** (Table S9 and S10). The exciton binding energies (E_c) from the ground state to the five excited states were calculated by density functional theory (DFT) calculations and time-dependent DFT (TD-DFT), and the results show that the exciton binding energies of **GDUT-8-Ox** are all smaller than those of **GDUT-8** highlighting greater charge separation efficiency of **GDUT-8-Ox** than **GDUT-8**, which is consistent with the results of the previous series of

characterizations. The difference in charge separation efficiency between **GDUT-8** and **GDUT-8-Ox** mainly originates from higher electrical conductivity (also faster electron transfer efficiency) of **GDUT-8-Ox** than **GDUT-8**. This ultimately manifests itself as a difference in photocatalytic activity.

To understand the mechanism of the photocatalytic reaction of MOFs, further density functional theory (DFT) calculations were done to determine the reaction mechanism of the CO_2 reduction to HCOOH reaction (Fig. 4a). **GDUT-8** and **GDUT-8-Ox** are mainly used for the reduction of CO_2 to HCOOH via the *OCHO pathway. Firstly, CO_2 is adsorbed and aggregated on the catalyst surface and the Gibbs free energy of **GDUT-8** and **GDUT-8-Ox** changes to -0.023 eV, indicating that CO_2 adsorption is spontaneous behavior. In the second CO_2 hydrogenation step, CO_2 acquires electrons from the Zr-O cluster to form an intermediate (*OCHO) and this step is the rate determining step for the reduction of CO_2 to HCOOH by **GDUT-8** and **GDUT-8-Ox**. The results showed that the energy stability of the intermediate formed by **GDUT-8-Ox** was 0.09 eV higher than that of **GDUT-8**, indicating that the formic acid was more easily formed. CO_2 then combined with H^+ and electrons once again to further form HCOOH, which was desorbed from the catalyst surface.

To probe any CO_2-derived reaction intermediates during photocatalytic CO_2RR, the reactions catalyzed by both **GDUT-8** and **GDUT-8-Ox** were monitored by *in-situ* FTIR spectroscopy. There are no significant changes in vibrational peaks of the *in- situ* FTIR spectra of both reactions under dark conditions in N_2 or CO_2 atmosphere and under light irradiation for 10 min in N_2 atmosphere (Fig. 4b and S48). After irradiation, at 1330, and 1478 cm^{-1} correspond to monodentate carboxylates (m-CO_3^{2-}).[42, 43] The absorption signals at 1551 and 1597 cm^{-1} were from bidentate carboxylates (b-CO_3^{2-}) while that at 1382 cm^{-1} stemmed from multi-dentate carboxylate (p-CO_3^{2-}). The presence of bicarbonate (HCO_3^-)[44-46] is confirmed by the absorption peaks at 1415 and 1448 cm^{-1}. [47] The absorption peaks of these carbonates intensified with time, indicating a possible interaction between CO_2 and water vapor.[48] The absorption signals at 1235, 1352 and 1641 cm-1 were assigned to the O-C-O symmetric stretching (ν_s), C-H bending, and O-C-O asymmetric stretching (ν_{as}) of *OCHO, [49] respectively (Fig.4b). And the peaks positions and vibrations states of the intermediate *OCHO of

GDUT-8-Ox and GDUT-8 are basically the same. Absorption peak from the intermediate *HCOOH (1690 cm^{-1}) [42] was also observed. The absorption peak at 1758 cm^{-1} arising from the $HCOO^-$ was found growing along with longer irradiation time and evidently support $HCOO^-$ as product of the photocatalytic CO_2RR.

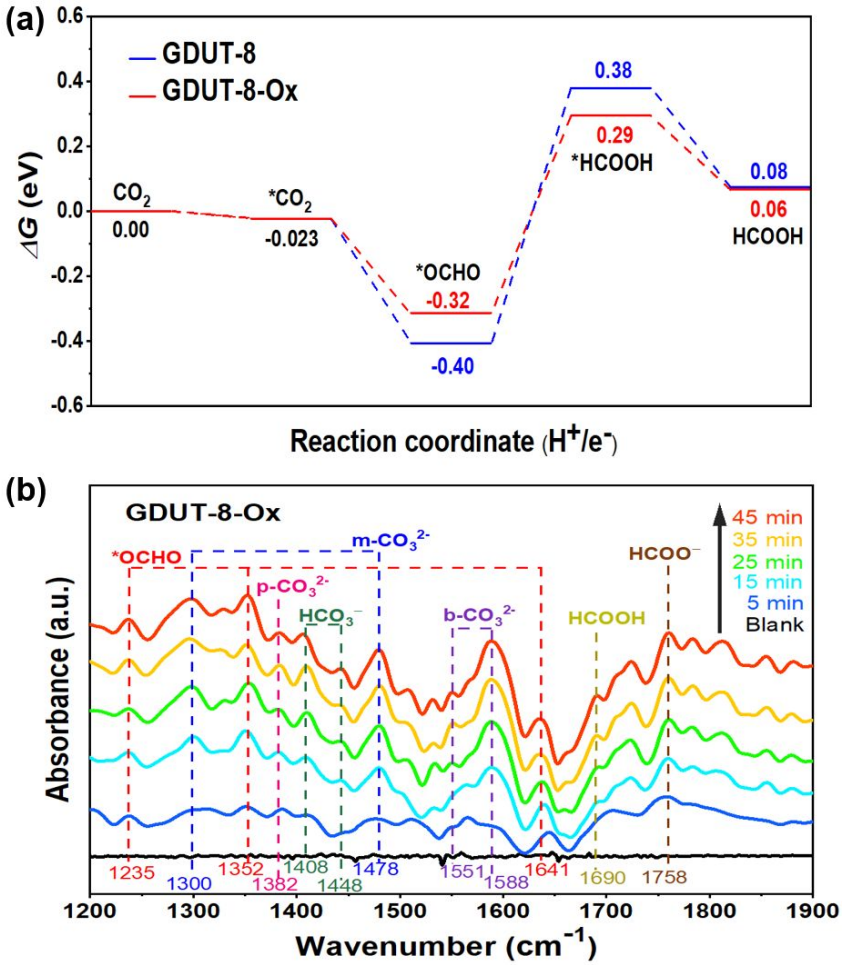

Fig. 4. (a) Calculated free-energy diagram for CO_2RR based on **GDUT-8-Ox**. (b) *In-situ* DRIFTS spectra for the reaction of CO_2 with H_2O on **GDUT-8-Ox** under visible light irradiation.

Supported by both experimental and theoretical results, the mechanism of CO_2-to-$HCOO^-$ reduction catalyzed by **GDUT-8** and **GDUT-8-Ox** under light irradiation is described below. Firstly, upon visible light irradiation, **BPD-4F4TS**$^{2-}$**/BPD-4F4TS-Ox**$^{4-}$ photo-excites to give a e^--h^+ pair state where photogenerated e^- migrate to the Zr–O cluster of **GDUT-8** /**GDUT-8-Ox**. After the Zr–O cluster accepts the electrons, Zr^{IV} is

reduced to Zr^{III}. In the Zr^{III} active site, CO_2 undergoes two steps to become $HCOO^-$. Firstly, CO_2 is converted to the intermediate *COOH which further reacts to give $HCOO^-$. Meanwhile, Zr^{III} serves as e^--donor and is oxidized back to Zr^{IV}. Compared with **GDUT-8**, coupled thiophene skeletons on **GDUT-8-Ox** form a stronger π-π conjugation with greater electron cloud densities, which contribute to faster e^- transfer to the Zr–O cluster. This probably accounts for better $HCOO^-$ formation from photocatalytic CO_2RR by **GDUT-8-Ox** than **GDUT-8**.

Conclusion

In summary, two Zr-based MOF catalysts, **GDUT-8** and **GDUT-8-Ox**, have been prepared based on $[Zr_6O_8]$ nodes and thiophene-functionalized biphenyl dicarboxylates. Noteworthy, **GDUT-8-Ox** bearing coupled thiophene linkers was obtained by Scholl reaction of **GDUT-8**. Coupling of adjacent thiophene pendants gave rise to improvement in electrical conductivity by at least two orders of magnitude (from 2.3×10^{-5} S cm^{-1} to 6.1×10^{-3} S cm^{-1}), leading to more facile transport of photogenerated carriers in **GDUT-8-Ox** than **GDUT-8**. Showing more pronounced LCCT efficiency and wider absorption profile (tailing extending from 400 nm to 800 nm), **GDUT-8-Ox** (1078 μmol g^{-1} h^{-1}) outperformed **GDUT-8** (533 μmol g^{-1} h^{-1}) in photocatalytic CO_2RR with $HCOO^-$ as the mere product (*i.e.*, 100% product selectivity). Remarkably, this work represents the first example to boost photocatalytic CO_2RR performance of MOF catalyst by promoting photogenerated charge carriers transfer/suppressing e^--h^+ pair recombination through betterment of the inherent electrical conductivity and undoubtedly opens a new avenue towards rational design of functional MOF catalysts for efficient photocatalytic CO_2RR.

Supporting Information

Supporting Information is available and includes the details of experimental instruments and measurement processes, synthesis of ligands, activation of crystal samples, DFT calculations results, crystallographic information and photocatalytic results and characterizations.

Conflict of Interest

The authors declare no conflict of interest.

Funding Information

This work was financially supported by the China Postdoctoral Science Foundation (2021M700877 and No. 15 Special Fund (In-Station), 2022T150143), the National Natural Science Foundation of China (No. 22201046, 21871061, and 21871141), the Local Innovative and Research Teams Project of Guangdong Pearl River Talents Program (2017BT01Z032).

Acknowledgments

Ning Li, Gui-Qi Lai and Lai-Hon Chung contributed equally to this work.

References

1. Zhao, Y. F.; Waterhouse, G. I. N.; Chen, G. B.; Xiong, X. Y.; Wu, L. Z.; Tung, C. H.; Zhang, T. R. Two-dimensional-related catalytic materials for solar-driven conversion of CO_x into valuable chemical feedstocks. *Chem. Soc. Rev.* **2019**, *48*, 1972-2010.

2. Ran, J. R.; Jaroniec, M.; Qiao, S. Z. Cocatalysts in Semiconductor-based Photocatalytic CO_2 Reduction: Achievements, Challenges, and Opportunities. *Adv. Mater.* **2018**, *30*, 1704649.

3. Xiao, J. D.; Li, R.; Jiang, H. L. Metal-Organic Framework-based Photocatalysis for Solar Fuel Production. *Small Methods*, **2023**, *66*, 436-442.

4. Huang, Q. S.; Wei, W.; Ni, B. J. Catalysts derived from Earth-abundant natural biomass enable efficient photocatalytic CO_2 conversion for achieving a closed-loop carbon cycle. *Green Chem.* **2021**, *23*, 9683-9692.

5. Ouyang, T.; Huang, H. H.; Wang, J. W.; Zhong, D. C.; Lu, T. B. A Dinuclear Cobalt Cryptate as a Homogeneous Photocatalyst for Highly Selective and Efficient Visible-Light Driven CO_2 Reduction to CO in CH3CN/H2O Solution. *Angew. Chem. Int. Ed.* **2017**, *56*, 738-743.

6. Wang, Q.; Warnan, J.; Rodriguez-Jimenez, S.; Leung, J. J.; Kalathil, S.; Andrei, V.; Domen, K.; Reisner, E. Molecularly engineered photocatalyst sheet for scalable solar formate production from carbon dioxide and water. *Nat. Energy* **2020**, *5*, 703-710.

7. Lu, K. Q.; Li, Y. H.; Zhang, F.; Qi, M. Y.; Chen, X.; Tang, Z. R.; Yamada, Y. M. A.; Anpo, M.; Conte, M.; Xu, Y. J. Rationally designed transition metal hydroxide nanosheet arrays on graphene for artificial CO_2 reduction. *Nat. Commun.* **2020**, *11,* 5181.

8. Fu, J. W.; Jiang, K. X.; Qiu, X. Q.; Yu, J. G.; Liu, M. Product selectivity of photocatalytic CO_2 reduction reactions. *Mater. Today* **2020**, *32*, 222-243.

9. Gong, E.; Ali, S.; Hiragond, C. B.; Kim, H. S.; Powar, N. S.; Kim, D.; Kim, H.; In, S. I. Solar fuels: research and development strategies to accelerate photocatalytic CO_2 conversion into hydrocarbon fuels. *Energy Environ. Sci.* **2022**, *15*, 880-937.

10. Zhang, H. B.; Wei, J.; Dong, J. C.; Liu, G. G.; Shi, L.; An, P. F.; Zhao, G. X.; Kong, J. T.; Wang, X. J.; Meng, X. G.; Zhang, J.; Ye, J. H. Efficient Visible-Light-Driven Carbon Dioxide Reduction by a Single-Atom Implanted Metal-Organic Framework. *Angew. Chem. Int. Ed.* **2016**, *55*, 14308-14312.

11. Qiu, Y. C.; Yuan, S.; Li, X. X.; Du, D. Y.; Wang, C.; Qin, J. S.; Drake, H. F.; Lan, Y. Q.; Jiang, L.; Zhou, H. C. Face-Sharing Archimedean Solids Stacking for the Construction of Mixed-Ligand Metal-Organic Frameworks. *J. Am. Chem. Soc.* **2019**, *141*, 13841-13848.

12. Dai, S.; Kajiwara, T.; Ikeda, M.; Romero-Muniz, I.; Patriarche, G.; Platero-Prats, A. E.; Vimont, A.; Daturi, M.; Tissot, A.; Xu, Q.; Serre, C. Ultrasmall Copper Nanoclusters in Zirconium Metal-Organic Frameworks for the Photoreduction of CO_2. *Angew. Chem. Int. Ed.* **2022**, *61*, e202211848.

13. Benseghir, Y.; Lemarchand, A.; Duguet, M.; Mialane, P.; Gomez-Mingot, M.; Roch-Marchal, C.; Pino, T.; Ha-Thi, M. H.; Haouas, M.; Fontecave, M.; Dolbecq, A.; Sassoye, C.; Mellot-Draznieks, C. Co-immobilization of a Rh Catalyst and a Keggin Polyoxometalate in the UiO-67 Zr-Based Metal-Organic Framework: In Depth Structural Characterization and Photocatalytic Properties for CO_2 Reduction. *J. Am. Chem. Soc.* **2020**, *142*, 9428-9438.

14. Qin, J. S.; Yuan, S.; Zhang, L.; Li, B.; Du, D. Y.; Huang, N.; Guan, W.; Drake, H. F.; Pang, J. D.; Lan, Y. Q.; Alsalme, A.; Zhou, H. C. Creating Well-Defined Hexabenzocoronene in Zirconium Metal-Organic Framework by Postsynthetic Annulation. *J. Am. Chem. Soc.* **2019**, *141*, 2054-2060.

15. Mahmoud, M. E.; Audi, H.; Assoud, A.; Ghaddar, T. H.; Hmadeh, M. Metal-Organic Framework Photocatalyst Incorporating Bis(4'-(4-carboxyphenyl)-terpyridine)ruthenium(II) for Visible-Light-Driven Carbon Dioxide Reduction. *J. Am. Chem. Soc.* **2019**, *141*, 7115-7121.

16. Gao, C.; Wang, J.; Xu, H. X.; Xiong, Y. J. Coordination chemistry in the design of heterogeneous photocatalysts. *Chem. Soc. Rev.* **2017**, *46*, 2799-2823.

17. Li, K.; Peng, B. S.; Peng, T. Y. Recent Advances in Heterogeneous Photocatalytic CO_2 Conversion to Solar Fuels. *ACS Catal.* **2016**, *6*, 7485-7527.

18. Chen, X. B.; Liu, L.; Yu, P. Y.; Mao, S. S. Increasing Solar Absorption for Photocatalysis with Black Hydrogenated Titanium Dioxide Nanocrystals. *Science* **2011**, *331*, 746-750.

19. Liu, G.; Pan, J.; Yin, L. C.; Irvine, J. T. S.; Li, F.; Tan, J.; Wormald, P.; Cheng, H. M. Heteroatom-Modulated Switching of Photocatalytic Hydrogen and Oxygen Evolution Preferences of Anatase TiO_2 Microspheres. *Adv. Funct. Mater.* **2012**, *22*, 3233-3238.

20. Wang, L.; Wan, Y. Y.; Ding, Y. J.; Wu, S. K.; Zhang, Y.; Zhang, X. L.; Zhang, G. Q.; Xiong, Y. J.; Wu, X. J.; Yang, J. L.; Xu, H. X. Conjugated Microporous Polymer Nanosheets for Overall Water Splitting Using Visible Light. *Adv. Mater.* **2017**, *29*, 1702428.

21. Dhakshinamoorthy, A.; Li, Z. H.; Garcia, H. Catalysis and photocatalysis by metal organic frameworks. *Chem. Soc. Rev.* **2018**, *47*, 8134-8172.

22. Gong, Y. N.; Zhong, W. H.; Li, Y.; Qiu, Y. Z.; Zheng, L. R.; Jiang, J.; Jiang, H. L. Regulating Photocatalysis by Spin-State Manipulation of Cobalt in Covalent Organic Frameworks. *J. Am. Chem. Soc.* **2020**, *142*, 16723-16731.

23. Chen, E. X.; Qiu, M.; Zhang, Y. F.; Zhu, Y. S.; Liu, L. Y.; Sun, Y. Y.; Bu, X. H.; Zhang, J.; Lin, Q. P. Acid and Base Resistant Zirconium Polyphenolate-Metalloporphyrin Scaffolds for Efficient CO_2 Photoreduction. *Adv. Mater.* **2018**, *30*, 1704388.

24. Xiao, J. D.; Jiang, H. L. Metal-Organic Frameworks for Photocatalysis and Photothermal Catalysis. *Acc. Chem. Res.* **2019**, *52*, 356-366.

25. Fang, Z. B.; Liu, T. T.; Liu, J. X.; Jin, S. Y.; Wu, X. P.; Gong, X. Q.; Wang, K. C.; Yin, Q.; Liu, T. F.; Cao, R.; Zhou, H. C. Boosting Interfacial Charge-Transfer Kinetics for Efficient Overall CO_2 Photoreduction via Rational Design of Coordination Spheres on Metal-Organic Frameworks. *J. Am. Chem. Soc.* **2020**, *142*, 12515-12523.

26. Li, N.; Liu, J.; Liu, J. J.; Dong, L. Z.; Xin, Z. F.; Teng, Y. L.; Lan, Y. Q. Adenine Components in Biomimetic Metal-Organic Frameworks for Efficient CO_2 Photoconversion. *Angew. Chem. Int. Ed.* **2019**, *58*, 5226-5231.

27. Dong, L. Z.; Zhang, L.; Liu, J.; Huang, Q.; Lu, M.; Ji, W. X.; Lan, Y. Q. Stable Heterometallic Cluster-Based Organic Framework Catalysts for Artificial Photosynthesis. *Angew. Chem. Int. Ed.* **2020**, *59*, 2659-2663.

28. Hendon, C. H.; Tiana, D.; Fontecave, M.; Sanchez, C.; D'Arras, L.; Sassoye, C.; Rozes, L.; Mellot-Draznieks, C.; Walsh, A. Engineering the Optical Response of the Titanium-MIL-125 Metal-Organic Framework through Ligand Functionalization. *J. Am. Chem. Soc.* **2013**, *135*, 10942-10945.

29. Grau-Crespo, R.; Aziz, A.; Collins, A. W.; Crespo-Otero, R.; Hernandez, N. C.; Rodriguez-Albelo, L. M.; Ruiz-Salvador, A. R.; Calero, S.; Hamad, S. Modelling a Linker Mix-and-Match Approach for Controlling the Optical Excitation Gaps and Band Alignment of Zeolitic Imidazolate Frameworks. *Angew. Chem. Int. Ed.* **2016**, *55*, 16012-16016.

30. Zhang, G. X.; Jin, L.; Zhang, R. X.; Bai, Y.; Zhu, R. M.; Pang, H. Recent advances in the development of electronically and ionically conductive metal-organic frameworks. *Coord. Chem. Rev.* **2021**, *439*, 213915.

31. Nasalevich, M. A.; van der Veen, M.; Kapteijn, F.; Gascon, J. Metal-organic frameworks as heterogeneous photocatalysts: advantages and challenges. *Crystengcomm* **2014**, *16*, 4919-4926.

32. Meng, H.; Perepichka, D. F.; Wudl, F. Facile solid-state synthesis of highly conducting poly(ethylenedioxythiophene). *Angew. Chem. Int. Ed.* **2003**, *42*, 658-661.

33. Rivnay, J.; Inal, S.; Collins, B. A.; Sessolo, M.; Stavrinidou, E.; Strakosas, X.; Tassone, C.; Delongchamp, D. M.; Malliaras, G. G. Structural control of mixed ionic and electronic transport in conducting polymers. *Nat. Commun.* **2016**, *7*, 11287.

34. Jones, A. L.; De Keersmaecker, M.; Savagian, L. R.; DiTullio, B. T.; Pelse, I.; Reynolds, J. R. Branched Oligo(ether) Side Chains: A Path to Enhanced Processability and Elevated Conductivity for Polymeric Semiconductors. *Adv. Funct. Mater.* **2021**, *31,* 2102688.

35. Cavka, J. H.; Jakobsen, S.; Olsbye, U.; Guillou, N.; Lamberti, C.; Bordiga, S.; Lillerud, K. P. A new zirconium inorganic building brick forming metal organic frameworks with exceptional stability. *J. Am. Chem. Soc.* **2008**, *130*, 13850-13851.

36. Li, R.; Zhang, W.; Zhou, K. Metal-Organic-Framework-Based Catalysts for Photoreduction of CO_2. *Adv. Mater.* **2018**, *30*, 1705512.

37. Liu, H.; Xu, C. Y.; Li, D. D.; Jiang, H. L. Photocatalytic Hydrogen Production Coupled with Selective Benzylamine Oxidation over MOF Composites. *Angew. Chem. Int. Ed.* **2018**, *57*, 5379-5383.

38. Xu, M. L.; Li, D. D.; Sun, K.; Jiao, L.; Xie, C. F.; Ding, C. M.; Jiang, H. L. Interfacial Microenvironment Modulation Boosting Electron Transfer between Metal Nanoparticles and MOFs for Enhanced Photocatalysis. *Angew. Chem. Int. Ed.* **2021**, *60*, 16372-16376.

39. Luo, Y. H.; Dong, L. Z.; Liu, J.; Li, S. L.; Lan, Y. Q. From molecular metal complex to metal-organic framework: The CO_2 reduction photocatalysts with clear and tunable structure. *Coord. Chem. Rev.* **2019**, *390*, 86-126.

40. Xu, H. Q.; Hu, J. H.; Wang, D. K.; Li, Z. H.; Zhang, Q.; Luo, Y.; Yu, S. H.; Jiang, H. L. Visible-Light Photoreduction of CO_2 in a Metal-Organic Framework: Boosting Electron-Hole Separation via Electron Trap States. *J. Am. Chem. Soc.* **2015**, *137*, 13440-13443.

41. Yan, Z. H.; Du, M. H.; Liu, J. X.; Jin, S. Y.; Wang, C.; Zhuang, G. L.; Kong, X. J.; Long, L. S.; Zheng, L. S. Photo-generated dinuclear {Eu(II)}(2) active sites for selective CO_2 reduction in a photosensitizing metal-organic framework. *Nat. Commun.* **2018**, *9, 3353*.

42. Liang, L.; Li, X. D.; Sun, Y. F.; Tan, Y. L.; Jiao, X. C.; Ju, H. X.; Qi, Z. M.; Zhu, J. F.; Xie, Y. Infrared Light-Driven CO_2 Overall Splitting at Room Temperature. *Joule* **2018**, *2*, 1004-1016.

43. Jiang, Z. F.; Sun, H. L.; Wang, T. Q.; Wang, B.; Wei, W.; Li, H. M.; Yuan, S. Q.; An, T. C.; Zhao, H. J.; Yu, J. G.; Wong, P. K. Nature-based catalyst for visible-light-driven photocatalytic CO_2 reduction. *Energy Environ. Sci.* **2018**, *11*, 2382-2389.

44. Chen, F.; Ma, Z. Y.; Ye, L. Q.; Ma, T. Y.; Zhang, T. R.; Zhang, Y. H.; Huang, H. W. Macroscopic Spontaneous Polarization and Surface Oxygen Vacancies Collaboratively Boosting CO_2 Photoreduction on $BiOIO_3$ Single Crystals. *Adv. Mater.* **2020**, *32*, 3353.

45. Zu, X. L.; Li, X. D.; Liu, W.; Sun, Y. F.; Xu, J. Q.; Yao, T.; Yan, W. S.; Gao, S.; Wang, C. M.; Wei, S. Q.; Xie, Y. Efficient and Robust Carbon Dioxide Electroreduction Enabled by Atomically Dispersed Sn delta$^+$ Sites. *Adv. Mater.* **2019**, *31*, 1808135.

46. Li, J.; Huang, H.; Xue, W.; Sun, K.; Song, X. Wu, C.; Nie, L.; Li, Y.; Liu, C.; Pan, Y.; Jiang, H. L.; Mei, D.; Zhong, C. Self-adaptive dual-metal-site pairs in metal-organic frameworks for selective CO_2 photoreduction to CH_4. *Nat. Catal.* **2021**, *4*, 719-729.

47. Yan, T. J.; Li, N.; Wang, L. L.; Ran, W. G.; Duchesne, P. N.; Wan, L. L.; Nguyen, N. T.; Wang, L.; Xia, M. K.; Ozin, G. A. Bismuth atom tailoring of indium oxide surface frustrated Lewis pairs boosts heterogeneous CO_2 photocatalytic hydrogenation. *Nat. Commun.* **2020**, *11*, 6095.

48. Zhou, J.; Li, J.; Kan, L.; Zhang, L.; Huang, Q.; Yan, Y.; Chen, Y. F.; Liu, J.; Li, S. L.; Lan, Y. Q. Linking oxidative and reductive clusters to prepare crystalline porous catalysts for photocatalytic CO_2 reduction with H_2O. *Nat. Commun.* **2022**, *13*, 4681.

49. Calatayud, M.; Collins, S. E.; Baltanás, M. A.; Bonivardi, A. L. Stability of formate species on β-Ga_2O_3. *Phys. Chem. Chem. Phys*. 2009, 11, 1397-1405.

Table of Contents Graphic